Autofocus for Event Cameras
-Supplemental Material-

Shijie Lin[1,5], Yinqiang Zhang[1,5], Lei Yu[2], Bin Zhou[3], Xiaowei Luo[4], Jia Pan[1]
[1]The University of Hong Kong [2]Wuhan University [3]Beihang University [4]City University of Hong Kong

Project page: https://eleboss.github.io/eaf_webpage/

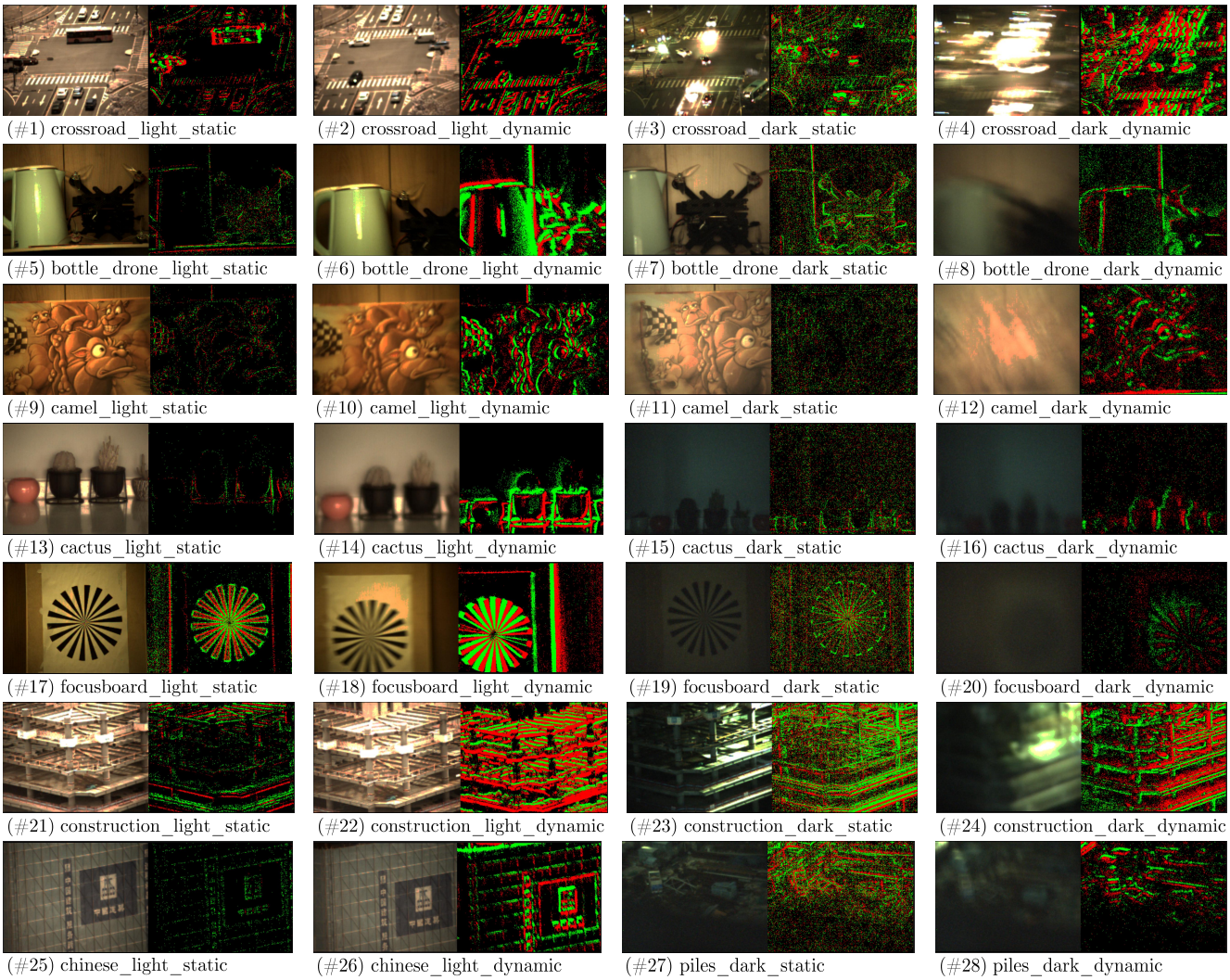

Figure 1. Examples of sequences in the proposed EAD. Images are screenshots of RGB frame (left) and event frame (right) captured at the optimal focal position.

Table 1. Details of the event-based autofocus dataset

ID	Scene	Images	Events	Lighting	Luminance	Indoor/Outdoor	Shaking motion	Name
1	Crossroad	641	412K	Light	14.3K Lux	Outdoor		crossroad_light_static
2	Crossroad	1025	13039K	Light	14.3K Lux	Outdoor	√	crossroad_light_dynamic
3	Crossroad	45	3809K	Dark	5.7 Lux	Outdoor		crossroad_dark_static
4	Crossroad	77	26198K	Dark	5.7 Lux	Outdoor	√	crossroad_dark_dynamic
5	Bottle & Drone	346	211K	Light	174.3 Lux	Indoor		bottle_drone_light_static
6	Bottle & Drone	402	11929K	Light	142 Lux	Indoor	√	bottle_drone_light_dynamic
7	Bottle & Drone	37	1493 K	Dark	3.25 Lux	Indoor		bottle_drone_dark_static
8	Bottle & Drone	59	13624K	Dark	2.49 Lux	Indoor	√	bottle_drone_dark_dynamic
9	Camel	240	84K	Light	168.1 Lux	Indoor		camel_light_static
10	Camel	559	7220 K	Light	168.1 Lux	Indoor	√	camel_light_dynamic
11	Camel	37	1186K	Dark	5.5 Lux	Indoor		camel_dark_static
12	Camel	54	9984K	Dark	5.5 Lux	Indoor	√	camel_dark_dynamic
13	Cactus	755	57K	Light	1308 Lux	Indoor		cactus_light_static
14	Cactus	1027	2942K	Light	1308 Lux	Indoor	√	cactus_light_dynamic
15	Cactus	39	1631K	Dark	0.7 Lux	Indoor		cactus_dark_static
16	Cactus	71	3617K	Dark	0.7 Lux	Indoor	√	cactus_dark_dynamic
17	Focus board	369	229K	Light	130 Lux	Indoor		focusboard_light_static
18	Focus board	489	16149K	Light	130 Lux	Indoor	√	focusboard_light_dynamic
19	Focus board	38	2365K	Dark	1.3 Lux	Indoor		focusboard_dark_static
20	Focus board	29	3194K	Dark	1.3 Lux	Indoor	√	focusboard_dark_dynamic
21	Construction sites	548	100K	Light	11.46K Lux	Outdoor		construction_light_static
22	Construction sites	805	10595K	Light	11.46K Lux	Outdoor	√	construction_light_dynamic
23	Construction sites	52	1986K	Dark	4.3 Lux	Outdoor		construction_dark_static
24	Construction sites	69	20020K	Dark	4.3 Lux	Outdoor	√	construction_dark_dynamic
25	Chinese characters	730	17K	Light	23.35K Lux	Outdoor		chinese_light_static
26	Chinese characters	960	735K	Light	23.35K Lux	Outdoor	√	chinese_light_dynamic
27	Piles of garbage	54	5772K	Dark	4.3 Lux	Outdoor		piles_dark_static
28	Piles of garbage	28	1291K	Dark	4.3 Lux	Outdoor	√	piles_dark_dynamic

Table 2. Quantitative comparisons in events of each sequence with the relative error

Sequence	GRAD [10]	WAVS [12]	SFIL [5]	LAP3 [1]	HELM [3]	GLLV [8]	EIGV [11]	DCTM [4]	CHEB [13]	SML [7]	ACMO [9]	ER ($\Delta t = 0.055$)	ER ($\Delta t = 0.065$)	ER + EGS
bottle_drone_dark_dynamic	-2160.0	-2160.0	-2160.0	-2160.0	1478.0	-2160.0	1478.0	-2153.0	1478.0	-2160.0	1477.0	140.0	127.0	66.0
bottle_drone_dark_static	-2155.0	-2155.0	-2155.0	-2155.0	1490.0	-2155.0	-2155.0	-2158.0	1477.0	-2155.0	-2159.0	77.0	89.0	-83.0
bottle_drone_light_dynamic	-2088.0	-2088.0	-2088.0	-2088.0	1555.0	-2088.0	1546.0	-1847.0	1555.0	-2088.0	-1383.0	168.0	118.0	-17.0
bottle_drone_light_static	-2360.0	-2360.0	-126.0	-2360.0	1271.0	-2363.0	-2362.0	400.0	1271.0	-2360.0	-2363.0	109.0	77.0	-86.0
cactus_dark_dynamic	-1644.0	-1644.0	-1644.0	-1644.0	1992.0	-1644.0	1936.0	-1643.0	1992.0	-1644.0	-1644.0	227.0	238.0	-236.0
cactus_dark_static	-1651.0	-1651.0	-1651.0	-1651.0	1987.0	-1651.0	-1651.0	-1652.0	1987.0	-1651.0	-1652.0	33.0	25.0	-19.0
cactus_light_dynamic	-1269.0	-1269.0	-1269.0	-1269.0	2368.0	-1268.0	-1269.0	-1260.0	2368.0	-1269.0	643.0	104.0	-46.0	45.0
cactus_light_static	-1459.0	-1459.0	-81.0	-1459.0	-762.0	-1459.0	2159.0	2159.0	2159.0	-1459.0	-1459.0	128.0	163.0	-137.0
camel_dark_dynamic	-2235.0	-2235.0	-2235.0	-2235.0	1360.0	-2235.0	-2235.0	744.0	1360.0	-2235.0	-2236.0	-42.0	-14.0	39.0
camel_dark_static	-2135.0	-2135.0	-2135.0	-2135.0	1504.0	-2135.0	-2124.0	-2103.0	1504.0	-2135.0	-2130.0	138.0	138.0	-155.0
camel_light_dynamic	-2152.0	-2152.0	-2152.0	-2152.0	1489.0	-2152.0	1489.0	-432.0	1488.0	-2152.0	232.0	55.0	-60.0	52.0
camel_light_static	-2147.0	-2147.0	-71.0	-2147.0	1497.0	-2148.0	1101.0	-334.0	1297.0	-2148.0	-2147.0	62.0	40.0	-12.0
chinese_light_dynamic	-683.0	-683.0	-683.0	-683.0	2957.0	-683.0	-683.0	126.0	-683.0	-683.0	95.0	79.0	90.0	-1.0
chinese_light_static	-707.0	-707.0	-707.0	-707.0	483.0	-707.0	2917.0	2917.0	2917.0	-707.0	-707.0	192.0	192.0	-191.0
construction_dark_dynamic	-1250.0	-1250.0	-1250.0	-1250.0	2369.0	-1246.0	2366.0	-755.0	2369.0	-1250.0	1980.0	-125.0	36.0	18.0
construction_dark_static	-1306.0	-1306.0	-1306.0	-1306.0	2336.0	-1306.0	2132.0	2334.0	2336.0	-1306.0	-1306.0	-99.0	-78.0	-44.0
construction_light_dynamic	-1437.0	-1437.0	-1437.0	-1437.0	2180.0	-1437.0	1066.0	-1439.0	2180.0	-1437.0	980.0	-177.0	44.0	-41.0
construction_light_static	-1358.0	-1358.0	-228.0	-1358.0	2282.0	-1356.0	2282.0	42.0	2282.0	-1358.0	-1358.0	-4.0	-45.0	9.0
crossroad_dark_dynamic	-1299.0	-1299.0	-1287.0	-1299.0	2343.0	-1289.0	2342.0	2343.0	2342.0	-1299.0	1988.0	-31.0	-21.0	32.0
crossroad_dark_static	-1274.0	-1274.0	-1274.0	-1274.0	2364.0	-572.0	1727.0	-1275.0	1624.0	-1274.0	-1275.0	-29.0	30.0	-44.0
crossroad_light_dynamic	-1602.0	-1602.0	-1600.0	-1602.0	2038.0	-1601.0	528.0	270.0	2038.0	-1602.0	1843.0	140.0	7.0	-23.0
crossroad_light_static	-1598.0	-1598.0	-1598.0	-1598.0	2040.0	-1597.0	-1440.0	313.0	-1597.0	-1598.0	229.0	-75.0	-56.0	50.0
focus_board_dark_dynamic	-2202.0	-2202.0	-2202.0	-2202.0	1437.0	-2202.0	-2202.0	1437.0	1437.0	-2202.0	-2201.0	12.0	18.0	-14.0
focus_board_dark_static	-2314.0	-2314.0	-2314.0	-2314.0	1326.0	-2314.0	-2313.0	-1637.0	1326.0	-2314.0	-2314.0	25.0	-7.0	6.0
focus_board_light_dynamic	-2209.0	-2208.0	-2208.0	-2209.0	1425.0	-2209.0	1423.0	-2174.0	1425.0	-2209.0	1343.0	-14.0	155.0	24.0
focus_board_light_static	-2250.0	-2250.0	-79.0	-2250.0	1377.0	-2250.0	1380.0	53.0	1377.0	-2250.0	-2250.0	120.0	67.0	-56.0
piles_dark_dynamic	-1269.0	-1269.0	-1269.0	-1269.0	2323.0	-1269.0	2323.0	-596.0	2323.0	-1269.0	-1275.0	35.0	16.0	49.0
piles_dark_static	-1242.0	-1242.0	-1242.0	-1242.0	2390.0	-1242.0	-1242.0	-268.0	2390.0	-1242.0	-1246.0	14.0	39.0	-28.0

Table 3. Cross-comparisons in events and frames of each sequence with the relative error

Sequence	GRAD [10]	WAVS [12]	SFIL [5]	LAP3 [1]	HELM [3]	GLLV [8]	EIGV [11]	DCTM [4]	CHEB [13]	SML [7]	ACMO [9]	ER ($\Delta t = 0.055$)	ER ($\Delta t = 0.065$)	ER + EGS
bottle_drone_dark_dynamic	257.0	-2160.0	-2159.0	-2160.0	1476.0	257.0	1476.0	-2161.0	-2155.0	-2161.0	-1207.0	140.0	127.0	66.0
bottle_drone_dark_static	141.0	141.0	141.0	141.0	141.0	141.0	1017.0	-2159.0	-1578.0	141.0	-2155.0	77.0	89.0	-83.0
bottle_drone_light_dynamic	95.0	95.0	321.0	95.0	162.0	95.0	1554.0	-163.0	-2089.0	95.0	-2083.0	168.0	118.0	-17.0
bottle_drone_light_static	25.0	25.0	25.0	25.0	-5.0	25.0	-770.0	234.0	-91.0	25.0	-2363.0	109.0	77.0	-86.0
cactus_dark_dynamic	-113.0	1991.0	-113.0	1992.0	1992.0	-113.0	-113.0	-1580.0	-1580.0	-1580.0	-1581.0	227.0	238.0	-236.0
cactus_dark_static	17.0	1985.0	17.0	17.0	17.0	17.0	17.0	373.0	17.0	-1651.0	-1651.0	33.0	25.0	-19.0
cactus_light_dynamic	-5.0	-5.0	-5.0	-5.0	-5.0	17.0	-5.0	-1268.0	-5.0	-5.0	1304.0	104.0	-46.0	45.0
cactus_light_static	-35.0	-55.0	-14.0	-55.0	-14.0	-14.0	-14.0	-383.0	-14.0	-55.0	-1458.0	128.0	163.0	-137.0
camel_dark_dynamic	-2235.0	-2235.0	178.0	-2235.0	178.0	-2235.0	-2235.0	1360.0	1360.0	-2235.0	-2235.0	-42.0	-14.0	39.0
camel_dark_static	146.0	146.0	146.0	146.0	146.0	146.0	708.0	-1022.0	146.0	146.0	-2135.0	138.0	138.0	-155.0
camel_light_dynamic	-7.0	-7.0	-7.0	-7.0	-7.0	-7.0	-498.0	-192.0	-7.0	-7.0	-2056.0	55.0	-60.0	52.0
camel_light_static	-4.0	-4.0	-4.0	-4.0	-4.0	-4.0	-79.0	-427.0	-4.0	-4.0	-2148.0	62.0	40.0	-12.0
chinese_light_dynamic	-24.0	-47.0	43.0	-24.0	-24.0	-24.0	43.0	117.0	-24.0	-24.0	98.0	79.0	90.0	-1.0
chinese_light_static	-46.0	-68.0	11.0	-68.0	-33.0	-9.0	-33.0	348.0	-9.0	-68.0	-462.0	192.0	192.0	-191.0
construction_dark_dynamic	99.0	99.0	-1249.0	99.0	99.0	-1244.0	-1248.0	1257.0	-1250.0	99.0	-1248.0	-125.0	36.0	18.0
construction_dark_static	118.0	118.0	118.0	118.0	118.0	118.0	-1305.0	2336.0	118.0	118.0	-1306.0	-99.0	-78.0	-44.0
construction_light_dynamic	-112.0	-165.0	-74.0	-165.0	-53.0	-11.0	1720.0	-1438.0	-132.0	-152.0	-1439.0	-177.0	44.0	-41.0
construction_light_static	-20.0	-74.0	40.0	-57.0	40.0	79.0	1014.0	-1343.0	17.0	-74.0	-1356.0	-4.0	-45.0	9.0
crossroad_dark_dynamic	132.0	132.0	365.0	132.0	132.0	-95.0	-1300.0	2342.0	2342.0	132.0	2342.0	-31.0	-21.0	32.0
crossroad_dark_static	84.0	84.0	84.0	84.0	84.0	558.0	2365.0	-1276.0	-1273.0	84.0	2364.0	-29.0	30.0	-44.0
crossroad_light_dynamic	47.0	-51.0	172.0	-51.0	-9.0	94.0	717.0	358.0	67.0	-51.0	-1602.0	140.0	7.0	-23.0
crossroad_light_static	87.0	11.0	156.0	11.0	102.0	156.0	671.0	156.0	87.0	11.0	-1598.0	-75.0	-56.0	50.0
focus_board_dark_dynamic	23.0	-567.0	23.0	-567.0	1437.0	23.0	1437.0	1437.0	23.0	-2180.0	-2200.0	12.0	18.0	-14.0
focus_board_dark_static	-2.0	-2.0	-2.0	-2.0	-2.0	-2.0	-2.0	1327.0	-2.0	-2.0	-2310.0	25.0	-7.0	6.0
focus_board_light_dynamic	109.0	24.0	109.0	24.0	-70.0	24.0	-70.0	622.0	109.0	24.0	1098.0	-14.0	155.0	24.0
focus_board_light_static	-71.0	-71.0	-39.0	-71.0	-71.0	-39.0	-2252.0	-134.0	-39.0	-71.0	-637.0	120.0	67.0	-56.0
piles_dark_dynamic	-91.0	241.0	-1273.0	241.0	-91.0	-1273.0	-1274.0	-1274.0	-1269.0	-1273.0	-1274.0	35.0	16.0	49.0
piles_dark_static	360.0	360.0	360.0	360.0	360.0	360.0	-1245.0	13.0	360.0	-1245.0	-1245.0	14.0	39.0	-28.0

1. Appendix

In the appendix, we show that why the intensity gradient can effectively capture the high-frequency information of intensity to reflect the degree of defocus.

1.1. Analysis of Defocusing and Focusing

The lens system can be conceptually modeled by the *thick lens* model, which follows the *Gaussian lens law*:

$$\frac{1}{d_o} + \frac{1}{d_i} = \frac{1}{f},$$

where d_o is the object distance, d_i is the image distance, f is the focal length. When the distance from the lens to sensor plane d_s equals image distance d_i, the sensor is properly focused, defocused otherwise. Let $\epsilon = |d_s - d_i|$ be the distance error, the change of object distance d_o changes d_i, thereby increasing the error ϵ and causing defocusing. The motorized varifocal lens can move the lens to reduce the distance error ϵ to refocus the system.

The relationship between the defocused intensity $I_d(x, y)$ and focused intensity $I_f(x, y)$ can be modelled using a 2-D Gaussian convolution [6]:

$$I_d(x, y) = h(x, y) * I_f(x, y), \tag{1}$$

where

$$h(x, y) = \frac{1}{2\pi\sigma_h^2} e^{-\frac{x^2+y^2}{2\sigma_h^2}}, \tag{2}$$

$h(x, y)$ is the Gaussian convolution kernel of defocusing, the σ_h is the spread parameter and is proportional to the distance error of focusing ϵ. In the frequency domain, we have:

$$I_D(u, v) = H(u, v) \cdot I_F(u, v), \tag{3}$$

where $I_D(u, v)$, $H(u, v)$ and $I_F(u, v)$ are the Fourier transforms of $I_d(x, y)$, $h(x, y)$ and $I_f(x, y)$ respectively, and $H(u, v)$ could be given by:

$$H(u, v) = e^{-\frac{u^2+v^2}{2}\sigma_h^2}. \tag{4}$$

When the degree of out-of-focus increases, the distance error ϵ increases, causing the increase of σ_h in Eq. (4), that is to say, the more defocus, the more the lens attenuates the high-frequency part of the focused intensity and blur the focused data. To automatically adjust the focal position of the lens, we need to measure the degree of defocus from data captured by cameras at different focal positions. This could be done by using the Sobel operator.

The Sobel operator is the approximation of the derivative of Gaussian filter [2], processing the defocused intensity with the Sobel operator is to convolve the defocused intensity with the derivatives of the Gaussian filter:

$$I_{sx}(x, y) = I_d(x, y) * \frac{dg_(x, y)}{dx}, \tag{5}$$

$$I_{sy}(x, y) = I_d(x, y) * \frac{dg_(x, y)}{dy}, \tag{6}$$

$g(x, y)$ is the inherent Gaussian filter of the Sobel operator. which can be given by:

$$g(x, y) = \frac{1}{2\pi\sigma_g^2} e^{-\frac{x^2+y^2}{2\sigma_g^2}} \tag{7}$$

In the frequency domain, Eq. (7) is:

$$G(u, v) = e^{-\frac{u^2+v^2}{2}\sigma_g^2}, \tag{8}$$

and Eq. (5) and Eq. (6) are:

$$\begin{aligned} I_{Sx}(u,v) &= I_D(u,v)\cdot(\boldsymbol{i}u)\cdot G(u,v), \\ &= I_D(u,v)\cdot(\boldsymbol{i}u)\cdot e^{-\frac{u^2+v^2}{2}\sigma_g^2}, \end{aligned} \tag{9}$$

$$\begin{aligned} I_{Sy}(u,v) &= I_D(u,v)\cdot(\boldsymbol{j}v)\cdot G(u,v), \\ &= I_D(u,v)\cdot(\boldsymbol{j}u)\cdot e^{-\frac{u^2+v^2}{2}\sigma_g^2}, \end{aligned} \tag{10}$$

where $\boldsymbol{i}$, and $\boldsymbol{j}$ are imaginary units, $I_{Sx}(u,v)$, $I_{Sy}(u,v)$, and $G(u,v)$ are Fourier transforms of $I_{sx}(x,y)$, $I_{sy}(x,y)$, and $g(x,y)$ respectively. The intensity after convolutions with Sobel operators $I_s(x,y)$ is:

$$I_s(x,y) = \sqrt{I_{sx}^2(x,y) + I_{sy}^2(x,y)}. \tag{11}$$

According to the discrete form of Parseval's theorem, the energy relationship of the intensity in spatial domains $I(x,y)$ and frequency domains $I(u,v)$ is:

$$\sum_{x=0}^{W}\sum_{y=0}^{H}|I(x,y)|^2 = \frac{1}{WH}\sum_{u}\sum_{v}|I(u,v)|^2, \tag{12}$$

where W and H are the width and height of the sensor plane, respectively. Applying Eq. (12) to $I_{sx}(x,y)$ and $I_{sy}(x,y)$, and sums them up, we have:

$$\sum_{x=0}^{W}\sum_{y=0}^{H}|I_{sx}(x,y)|^2 + |I_{sy}(x,y)|^2 = \frac{1}{WH}\sum_{u}\sum_{v}|I_{Sx}(u,v)|^2 + |I_{Sy}(u,v)|^2. \tag{13}$$

Applying Eq. (11) to the left of Eq. (13), then relating Eq. (9), and Eq. (10) to the right of Eq. (13), we have:

$$\sum_{x=0}^{W}\sum_{y=0}^{H}|I_s(x,y)|^2 = \frac{1}{WH}\sum_{u}\sum_{v}\left(u^2+v^2\right)\cdot e^{-\left(u^2+v^2\right)\sigma_g^2}\cdot|I_D(u,v)|^2. \tag{14}$$

Finally, by putting Eq. (3) in Eq. (14), we have the energy relationship of intensity gradient in spatial and frequency domains:

$$\sum_{x=0}^{W}\sum_{y=0}^{H}|I_s(x,y)|^2 = \frac{1}{WH}\sum_{u}\sum_{v}\left(u^2+v^2\right)\cdot e^{-\left(u^2+v^2\right)\left(\sigma_h^2+\sigma_g^2\right)}\cdot|I_{\mathrm{F}}(u,v)|^2. \tag{15}$$

In Eq. (15), there are two important terms. The first term is u^2+v^2, a second-order parabola in the frequency domain and stays unchanged. The second terms is $e^{-\left(u^2+v^2\right)\left(\sigma_h^2+\sigma_g^2\right)}$. In the second term, σ_h is introduced by defocus, which changes following the degree of defocus, σ_g is introduced by the Sobel operator and stays unchanged. So we can see that the first term is the differential term that removes the DC component in the intensity, changes the band frequency component, and does not change with the σ_h. In the second term, all band frequency components decrease monotonously with the increase of σ_h. Therefore, the energy of the gradient decreases monotonically with the increase of σ_h. In the spatial domain, the gradient of the intensity, *i.e.*, $I_s(x,y)$ decreases monotonically with the increase of σ_h. As σ_h is linearly proportional to the distance error of focusing ϵ, we successfully established the relationship between the intensity gradient and the ϵ. This relationship shows that the intensity gradient computed using the Sobel operator can properly reflect the degree of defocus.

1.2. Complexity Analysis

The complexity of focus measure ER is $\mathcal{O}(N_e)$ as it is a simple event counting operator. Regarding EGS, we only have to calculate ER once and then implement the Goden section search algorithm, which is efficient and only has complexity of $\mathcal{O}(N_e)$. The runtime curves of ER (Fig. 2b) and EGS (Fig. 2a) verify the linear complexity of our methods. Noted that EGS is very efficient ($<$10 ms for 3 million events).

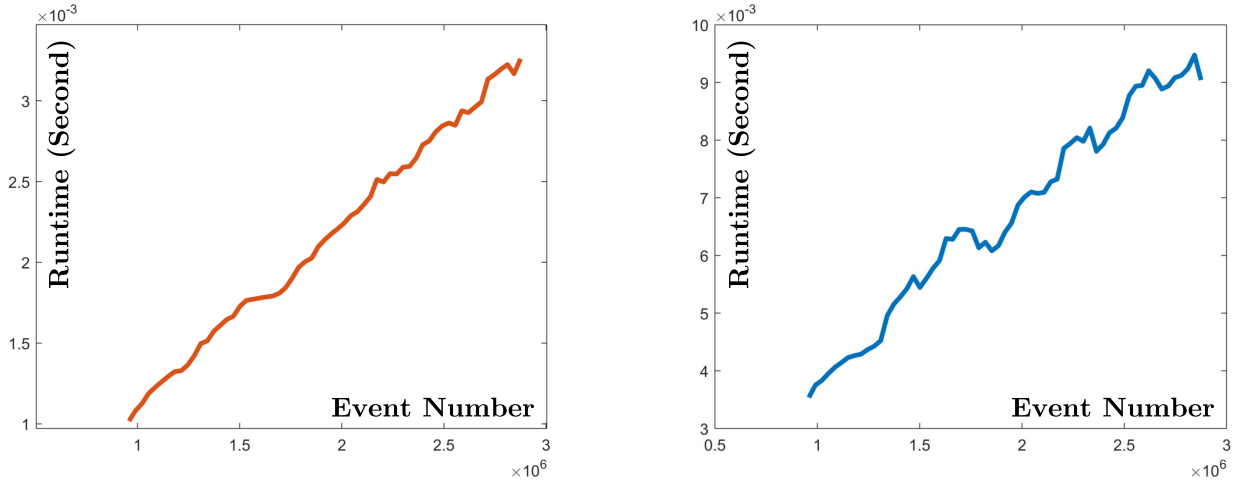

(a) Runtime of ER

(b) Runtime of EGS

Figure 2. Runtime of ER and EGS computed using the sequence: *focus_board_dark_dynamic*. We randomly sample events in this sequence to generate a subset and measure the computing time of our algorithms in this subset. As we gradually increase the size of the subset, we can see that the runtime of our algorithm is linear to the event number.

1.3. Failure Cases Analysis

In the main content of the paper, we provide the averaged mean square error and root mean square error for general results. In this appendix, we provide the full results of all sequences using the relative error, which is more effective in demonstrating whether or not our algorithm has near/far bias. The quantitative comparisons in events with the relative error of each sequence are shown in Tab. 2 and cross-comparisons in events and frames are shown in Tab. 3. In Tab. 2, we can see that due to the event noise, previous methods cannot properly operate on the event frame, resulting in large errors.

From Tab. 3, we can see that our ER+EGS gains relatively large error in *camel_dark_static* (-155), *chinese_light_static* (-191), and *cactus_light_static* (-137.0). The reason is a combination of noise and the simplicity of the scenes. In simple scenes, contrast variations are low, generating fewer events. Due to a relatively low signal-noise ratio, the real ER peak value can hardly distinguish itself from surrounding measurements. Our EGS starts with large intervals contaminated by noise, and as the peak is not sharp enough, noise creates several suboptimal results, making EGS ultimately converges to one of them.

For the dynamic case *cactus_dark_dynamic* (-236.0), the shaking motion is too large, breaking the assumption that the field of view should be constrained to the consistent targets during focusing, leading to other optimal points being focused. Most frame-based methods work well in images captured under static scenes with comfort lighting. But in dynamic scenes with poor lighting conditions, these frame-based methods fails heavily (*e.g.*, 257 *vs*. 66 in *bottle_drone_dark_dynamic*).

References

[1] Youngeun An, Gwangwon Kang, Il-Jung Kim, Hyun-Sook Chung, and Jongan Park. Shape from focus through laplacian using 3d window. In *2008 Second International Conference on Future Generation Communication and Networking*, volume 2, pages 46–50, 2008. 3, 4

[2] Rafael C Gonzalez and Richard E Woods. Digital image processing, hoboken, 2018. 5

[3] Franz Stephan Helmli and Stefan Scherer. Adaptive shape from focus with an error estimation in light microscopy. In *Proceedings of the 2nd International Symposium on Image and Signal Processing and Analysis*, pages 188–193, 2001. 3, 4

[4] Sang-Yong Lee, Yogendera Kumar, Ji-Man Cho, Sang-Won Lee, and Soo-Won Kim. Enhanced autofocus algorithm using robust focus measure and fuzzy reasoning. *IEEE Transactions on Circuits and Systems for Video Technology*, 18(9):1237–1246, 2008. 3, 4

[5] Rashid Minhas, Abdul A Mohammed, QM Jonathan Wu, and Maher A Sid-Ahmed. 3d shape from focus and depth map computation using steerable filters. In *International conference image analysis and recognition*, pages 573–583. Springer, 2009. 3, 4

[6] Shree K Nayar and Yasuo Nakagawa. Shape from focus: An effective approach for rough surfaces. In *Proceedings., IEEE International Conference on Robotics and Automation (ICRA)*, pages 218–225, 1990. 5

[7] Shree K Nayar and Yasuo Nakagawa. Shape from focus. *IEEE Transactions on Pattern analysis and machine intelligence*, 16(8):824–831, 1994. 3, 4

[8] José Luis Pech-Pacheco, Gabriel Cristóbal, Jesús Chamorro-Martinez, and Joaquín Fernández-Valdivia. Diatom autofocusing in brightfield microscopy: a comparative study. In *Proceedings 15th International Conference on Pattern Recognition (ICPR)*, volume 3, pages 314–317, 2000. 3, 4

[9] Mukul V Shirvaikar. An optimal measure for camera focus and exposure. In *Thirty-Sixth Southeastern Symposium on System Theory, 2004. Proceedings of the*, pages 472–475, 2004. 3, 4

[10] Jay Martin Tenenbaum. *Accommodation in computer vision*. Stanford University, 1971. 3, 4

[11] Chong-Yaw Wee and Raveendran Paramesran. Measure of image sharpness using eigenvalues. *Information Sciences*, 177(12):2533–2552, 2007. 3, 4

[12] Ge Yang and Bradley J Nelson. Wavelet-based autofocusing and unsupervised segmentation of microscopic images. In *Proceedings of IEEE/RSJ International Conference on Intelligent Robots and Systems (IROS)*, volume 3, pages 2143–2148, 2003. 3, 4

[13] Pew Thian Yap and P Raveendran. Image focus measure based on chebyshev moments. *IEE Proceedings-Vision, Image and Signal Processing*, 151(2):128–136, 2004. 3, 4